On the calculation of dynamical properties of solvated electrons by maximum entropy analytic continuation of path integral Monte Carlo data

E. Gallicchio and B. J. Berne
Department of Chemistry, Columbia University, New York, New York 10027

(Received 15 May 1996; accepted 17 July 1996)

The maximum entropy analytic continuation method, to determine the dynamical properties of a solvated electron from equilibrium path integral Monte Carlo data, is applied to the calculation of the optical absorption spectra, real time correlation functions, and transport coefficients of an excess electron in water, supercritical helium, and supercritical xenon. Comparisons with experiments and with analytical theories are presented. © *1996 American Institute of Physics.* [S0021-9606(96)51540-0]

I. INTRODUCTION

In many condensed phases, ranging from ionic liquids to polar and nonpolar molecular liquids, and under a broad range of thermodynamic conditions it is possible to observe a stable low-energy electron in thermal equilibrium with the surrounding solvent. Such excess electrons can be introduced into a liquid either by photoionization or by injection by a low-energy electron beam. Once thermalized, the excess electron can be in a localized or extended state and often behaves differently than the valence electrons of the solvent molecules.

Excess electrons can be monitored by a number of different techniques most of which, such as optical absorption, photoelectric spectroscopy, and photoconductivity, probe the dynamics of thermalized solvated electrons.[1] These quantities, however, are also the most difficult to determine from realistic many-body theoretical models and, consequently, several of the experimental findings cannot be used to quantitatively test and improve our present theoretical understanding of the phenomenon of electron solvation.

Path integral Monte Carlo (PIMC) methods[2] have been extensively used to determine the equilibrium structure and solvation energies of excess electrons in various fluids. These methods allow accurate numerical determination of equilibrium properties and time correlation functions as a function of imaginary time. Although important in elucidating some of the properties of the excess electron, these numerical studies have not given accurate information about dynamical properties like the electron conductivity, the optical absorption coefficient, and the behavior of real-time correlation functions. Besides, the direct real-time Monte Carlo simulation of these quantum dynamical quantities is not feasible because of the phase cancellation problem.[3]

There has been considerable progress in simulating the dynamics of solvated electron systems by quantum molecular dynamics (QMD), both for the adiabatic[4] and nonadiabatic regime,[5,6] however, such methods may be impractical for the determination of equilibrium dynamical properties derived from time correlation functions because they require averaging over a large number of trajectories and they do not efficiently sample high-energy states, giving rise to the tail of the absorption spectrum. In their present form, besides, these methods cannot go beyond the classical treatment of the solvent degrees of freedom.

A different approach to this problem is based on the Baym and Mermin theorem[7] that shows that real-time quantum correlation functions are analytical continuations of imaginary time correlation functions to the real-time axis (Wick rotations). Although the imaginary time correlation functions are readily available from PIMC calculations, even for fairly complex systems, in practice, the numerical analytic continuation operation has to be carried out with great care because it is known to be very unstable and capable of enormously amplifying the unavoidable statistical errors of the imaginary-time correlation function. In recent years, however, maximum entropy image enhancement techniques[8] have been successfully applied to solve a variety of ill-conditioned problems[9,10] and, in particular, to effect a stable numerical analytical continuation of imaginary-time correlation functions of several systems.[11–3] We have recently tested this methodology on a simple, exactly solvable, model system related to the self-trapped electron in a fluid and we have applied it to the calculation of the optical absorption spectrum of an excess electron in supercritical helium.[14]

One of the strengths of this method is that, for its implementation, no approximations are required. In particular, the method allows the study of electron dynamics in quantum solvents, thereby including nonadiabatic effects, and, thus, allowing simulations to go beyond the mixed quantum-classical ensembles.

In this paper we apply the maximum entropy analytic continuation method to the study of the adiabatic dynamics of an excess electron in various solvents. The methodology used in the previous study[14] has been extended to include recent developments in the maximum entropy algorithms[8,15] and we also present a scheme for the determination of the real-time correlation function and transport coefficients omitted in the previous work[14] that was focused mainly on the calculation of the optical absorption spectra.

In the next section we derive an analytic continuation scheme for the displacement correlation function $\langle|\mathbf{r}(t)-\mathbf{r}(t')|^2\rangle$ by means of an integral equation that relates

 0021-9606/96/105(16)/7064/15/$10.00

the imaginary-time displacement correlation function to the optical absorption cross section. In Sec. III we outline the maximum entropy method and its application to the numerical solution of the integral equation derived in Sec. II. In Sec. IV we review the PIMC method used to obtain the equilibrium quantities and the imaginary-time correlation function needed as input to the analytic continuation scheme. In Sec. V we apply the proposed method to estimate the optical absorption cross section, the real-time displacement correlation function, and the real-time velocity autocorrelation function of an excess electron in liquid water at different thermodynamic conditions; we compare the calculated absorption spectra in water to the available experimental findings and we find good agreement. In Sec. VI we calculate the absorption spectra, real-time displacement correlation functions, and diffusion constants of an excess electron in supercritical helium at medium and low densities, we compare our calculations with analytical results for the associated hard sphere model and we find reasonable agreement. In Sec. VII we investigate the possibility, using the proposed method, to reproduce the experimental conductivity data of excess electrons in xenon; we find only qualitative agreement with the experiments, we propose an explanation for the observed deviations, and we discuss the implications for future applications of the method. In Sec. VIII we finally present some concluding remarks.

II. OPTICAL ABSORPTION AND REAL-TIME DYNAMICS

The dipole time autocorrelation function of a system with Hamiltonian H at the inverse temperature $\beta=1/k_{\mathrm{B}}T$ (k_{B} is the Boltzmann constant) is

$$C(t)=\langle \boldsymbol{\mu}(t)\cdot\boldsymbol{\mu}(0)\rangle=\frac{\mathrm{Tr}(e^{-\beta H}e^{itH/\hbar}\boldsymbol{\mu}\cdot e^{-itH/\hbar}\boldsymbol{\mu})}{\mathrm{Tr}(e^{-\beta H})}, \quad (1)$$

where $\boldsymbol{\mu}$ is the dipole operator of the system. The dipole spectral density function $I(\omega)$ is defined as the Fourier transform of $C(t)$, namely

$$I(\omega)=\int_{-\infty}^{+\infty} dt\ e^{i\omega t}C(t), \quad (2)$$

and the absorption cross section,

$$\sigma(\omega)=\frac{4\pi}{\hbar c}\,\omega(1-e^{-\beta\hbar\omega})I(\omega), \quad (3)$$

describes the absorption of a monochromatic radiation of frequency ω due to the interaction with the dipole of the system.[16]

The dipole moment of the solvated electron is $\boldsymbol{\mu}=-|e|\mathbf{r}$, where e is the electron charge and $\mathbf{r}$ the electron position, so that

$$C(t)=e^2\langle \mathbf{r}(t)\cdot\mathbf{r}(0)\rangle. \quad (4)$$

Inverting Eq. (2), expressing the dipole autocorrelation function in terms of the time-ordered displacement correlation function for $t\geqslant 0$,

$$R_T^2(t)=\langle \hat{T}(|\mathbf{r}(t)-\mathbf{r}(0)|^2)\rangle=\frac{2}{e^2}\,[C(0)-C(t)], \quad (5)$$

where $\hat{T}$ is the time-ordering operator, one finds

$$e^2R_T^2(t)=\int_{-\infty}^{+\infty}\frac{d\omega}{\pi}\,I(\omega)(1-e^{-i\omega t}). \quad (6)$$

Finally, introducing the detailed balance relation $I(-\omega)=e^{-\beta\hbar\omega}I(\omega)$ and the absorption cross section in Eq. (3), Eq. (6) can be written in the form

$$\frac{4\pi^2e^2}{\hbar c}\,R_T^2(t)=\int_0^{\infty} d\omega\ \sigma(\omega)\times\frac{\cosh(\beta\hbar\omega/2)-\cosh[\beta\hbar\omega(\frac{1}{2}-it/\beta\hbar)]}{\omega\ \sinh(\beta\hbar\omega/2)}. \quad (7)$$

A time-ordered correlation function is an analytic function in the complex plane; thus, it can be expressed in Euclidean time τ by performing the substitution $t\rightarrow -i\tau$, where $0\leqslant\tau\leqslant\beta\hbar$.[7] Applying this to Eq. (7), we obtain

$$\frac{4\pi^2e^2}{\hbar c}\,R_T^2(-i\tau)=\int_0^{\infty} d\omega\ \sigma(\omega)K(\omega,\tau), \quad (8)$$

where

$$K(\omega,\tau)=\frac{\cosh(\beta\hbar\omega/2)-\cosh[\beta\hbar\omega(\frac{1}{2}-\tau/\beta\hbar)]}{\omega\ \sinh(\beta\hbar\omega/2)}. \quad (9)$$

Equation (8) is an integral equation that relates the Euclidean-time displacement correlation function and the absorption cross section, $\sigma(\omega)$, through the kernel function $K(\omega,\tau)$ defined in Eq. (9).

In the following we will omit the time-ordering subscript T when it refers to the Euclidean-time correlation function $R_T^2(-i\tau)$ with the convention that the imaginary-time parameter τ is real and positive.

The numerical calculation of the imaginary-time displacement correlation function $R^2(-i\tau)$ is feasible, even for fairly complicated systems while the calculation of the corresponding real-time function is often infeasible because of the phase cancellation problem,[3] thus, in principle, the inversion of the integral equation (8) provides a method for obtaining dynamical information, like the absorption spectrum, inaccessible by other means. It should be noted, however, that the numerical inversion of Eq. (8) is a very unstable operation—the systematic and the unavoidable statistical errors on the imaginary-time displacement correlation function $R^2(-i\tau)$ are enormously amplified in the absorption spectrum $\sigma(\omega)$—and therefore the inversion must be performed very carefully. The numerical inversion method we have chosen to use is described in Sec. III.

It should be noted that the kernel function $K(\omega,\tau)$ in Eq. (9) is proportional to the imaginary-time displacement correlation function of a harmonic oscillator of frequency ω and mass m

$$R^2(-i\tau)_{\text{h.o.}}=\frac{3\hbar}{m\omega\,\sinh(\beta\hbar\omega/2)}\left\{\cosh\left(\frac{\beta\hbar\omega}{2}\right)-\cosh\left[\beta\hbar\omega\left(\frac{1}{2}-\frac{\tau}{\beta\hbar}\right)\right]\right\}. \tag{10}$$

Thus, Eq. (8) states that $R^2(-i\tau)$ can be expressed as a linear superposition of harmonic components. In this interpretation, therefore, the differential absorption intensity $d\omega\ \sigma(\omega)$ measures the contribution of the harmonic component of frequency ω to the total imaginary-time displacement correlation function. By the inverse argument, therefore, the solution of Eq. (8) for a harmonic oscillator of frequency ω_0 must be, as expected, proportional to a δ function at ω_0. It can be also noted that the singularity of $K(\omega,\tau)$ at $\omega=0$ can be easily removed by observing that

$$\lim_{\omega\to 0} K(\tau,\omega)=\frac{\tau(\beta\hbar-\tau)}{\beta\hbar}, \tag{11}$$

which is proportional to the imaginary-time displacement correlation function of a free particle, i.e., of a harmonic oscillator of infinitely small frequency.

The first and second derivatives of the imaginary-time displacement correlation functions $R^2(-i\tau)$ at $\tau=0^+$ can be related, respectively, to the initial values of the velocity–position and velocity–velocity correlation functions

$$\left.\frac{dR^2(-i\tau)}{d\tau}\right|_{\tau=0^+}=2i\langle\mathbf{v}\cdot\mathbf{r}\rangle \tag{12}$$

and

$$\left.\frac{d^2R^2(-i\tau)}{d\tau^2}\right|_{\tau=0^+}=-2\langle\mathbf{v}\cdot\mathbf{v}\rangle. \tag{13}$$

By differentiating Eq. (8) with respect to τ and using the relations above, we have

$$\frac{\hbar c}{4\pi^2 e}\int_0^\infty d\omega\ \sigma(\omega)=2i\langle\mathbf{v}\cdot\mathbf{r}\rangle \tag{14}$$

and

$$\frac{\hbar c}{4\pi^2 e}\int_0^\infty d\omega\ \frac{\omega\sigma(\omega)}{\tanh(\beta\hbar\omega/2)}=2\langle|v|^2\rangle, \tag{15}$$

which are two sum rules for the absorption cross section $\sigma(\omega)$.

Once the absorption cross section is known by inverting Eq. (8), the analytic continuation of $R_T^2(t)$ from the negative imaginary axis to the positive real-time axis can be completed by performing the integration in Eq. (7). The real-time displacement correlation function $R^2(t)=\langle|\mathbf{r}(t)-\mathbf{r}(0)|^2\rangle$ is equal to the real part of $R_T^2(t)$. Other real-time correlation functions can be extracted from $\sigma(\omega)$, for instance the velocity autocorrelation function for $t\geqslant 0$ can be calculated using the relation

$$\langle\mathbf{v}(t)\cdot\mathbf{v}\rangle=-\frac{d^2}{dt^2}\langle\mathbf{r}(t)\cdot\mathbf{r}\rangle,\quad t\geqslant 0, \tag{16}$$

and Eqs. (4), (5), and (7), obtaining

$$\frac{8\pi^2e^2}{\hbar c}\langle\mathbf{v}(t)\cdot\mathbf{v}\rangle=\int_0^\infty d\omega\ \omega\sigma(\omega)\times\frac{\cosh[\beta\hbar\omega(\frac{1}{2}-it/\beta\hbar)]}{\sinh(\beta\hbar\omega/2)}. \tag{17}$$

The diffusion coefficient D of the electron is defined as[17]

$$D=\lim_{t\to\infty}\frac{R^2(t)}{6t} \tag{18}$$

$$=\lim_{s\to 0}\frac{1}{3}\int_0^\infty dt\ e^{-st}\langle\mathbf{v}(t)\cdot\mathbf{v}\rangle. \tag{19}$$

By substituting either Eq. (7) or Eq. (17) and using the fact that[18]

$$\frac{1}{\pi}\lim_{t\to\infty}\frac{1-\cos\,\omega t}{\omega^2 t}=\frac{1}{\pi}\lim_{s\to 0}\frac{1}{s(1+\omega^2/s^2)}=\delta(\omega), \tag{20}$$

it can be shown that the diffusion coefficient is proportional to the zero-frequency absorption, namely

$$D=\frac{\hbar c}{4\pi}\frac{\sigma(0)}{6e^2\beta\hbar}=\frac{c}{24\pi e^2\beta}\,\sigma(0). \tag{21}$$

III. THE MAXIMUM ENTROPY INVERSION METHOD

In order to perform the analytical continuation of the imaginary-time displacement correlation function, the numerical solution of the integral equation (8) is required. The inversion of this integral equation is like the inversion of a Laplace transform because it basically involves the problem of resolving a noisy signal that is composed of a sum of exponential decays: a well-known ill-conditioned problem. As a consequence, $R^2(-i\tau)$ is rather insensitive to the details of $\sigma(\omega)$ so that it is always possible to adjust amplitudes and frequencies to obtain virtually perfect fits to the calculated data, but often these amplitudes and frequencies are far from being unique. The severity of this problem means that the noisy datasets contain limited amounts of information about the spectrum. It is necessary, therefore, to incorporate prior knowledge to limit the range of possible solutions.

A variety of numerical inversion methods based on this principle are available.[19–23] In these methods the least-square deviation of the fit is minimized subject to a number of constraints that contain information about such known properties of the spectrum as positivity and sum rules or assumptions about smoothness. Each constraint is then associated with an undetermined Lagrange multiplier. Such methods are all implementations of the basic concept of *Maximum Likelihood*.[24] The maximum entropy method (MEM)[25,26] is based on the complementary concept of *Maximum Entropy*.[24] The maximum entropy method approaches the problem of data analysis from information and probability theory and is based on well-established mathematical axioms. While the maximum likelihood method approach selects the spectrum that has the largest probability of reproducing the data, the

maximum entropy method, instead, selects the positive spectrum to which is associated the largest number of ways of reproducing the data, i.e., the one that maximizes the information-theory definition of the entropy of the spectrum subject to the given constraints.

The inversion problem is reduced by the maximum entropy method to finding the maximum of the entropy given a constraint on the value of the least-square deviation from the data. In this paper the resulting Lagrange multiplier is selected according to the classic maximum entropy[8,15] scheme in which the Lagrange multiplier is determined self-consistently, and therefore the method has no adjustable parameters. The most important feature of the maximum entropy approach is the fact that, since the solution has the minimum information content, any structure present in the spectrum must be due to the data. Another useful feature of the method is that it allows the introduction of prior known information about the solution through a default spectrum. Last, the method is able to estimate the reliability of the inversion.[13]

The following is a brief account of the maximum entropy method in its application to the analytic continuation method; for a more detailed description the reader is referred to existing publications.[27]

The maximum entropy inversion method is applicable to the general problem of evaluating a set of unknowns from a dataset, knowing only the rule that generates the data from the unknowns. The inverse operation is never invoked and it can be assumed unavailable. We will focus on the numerical solution of the integral equation,

$$D(\tau)=\int d\omega\ K(\tau,\omega)A(\omega), \tag{22}$$

where $D(\tau)$ represents the calculated or measured data, $A(\omega)$ is a positive unknown function called the *map*, and $K(\tau,\omega)$ is a regular kernel function. In practice, $D(\tau)$ is known only on a discrete set of points $D_i=D(\tau_i)$, $i=1,\ldots,M$. To every D_i is also assigned an uncertainty σ_i. Analogously, we look for the values of $A(\omega)$ on the set of points ω_j, $j=1,\ldots,N$ and we carry out the integration in the finite interval $\omega_{\min}\leqslant\omega\leqslant\omega_{\max}$, implicitly assuming $A(\omega)=0$ outside this interval. We also assume for the moment that the data are uncorrelated, i.e., that the D_i's can be considered independent variables. Later we will drop this assumption.

The maximum entropy method assigns to the map $A(\omega)$ a probability distribution that is dependent on the data available, and defines the solution $A(\omega)$ of Eq. (22) as the most probable map. Let $\mathscr{P}(A|D)$ be the probability of the map A given the data D. By Bayes theorem

$$\mathscr{P}(A|D)\propto\mathscr{P}(A)\mathscr{P}(D|A); \tag{23}$$

where $\mathscr{P}(A)$ is the so-called *prior* probability for A, i.e., the probability distribution we assign to A before acquiring the data, and $\mathscr{P}(D|A)$ is the *likelihood* probability, i.e., the probability of obtaining the data D by the transformation (22) with the given map A.

The prior distribution for the map is taken to be

$$\mathscr{P}(A|\alpha,m)\propto e^{\alpha S}, \tag{24}$$

where α is an arbitrary positive parameter, S is the entropy function,

$$S=\sum_{j=1}^{N}\left(A_j-m_j-A_j\ \ln\frac{A_j}{m_j}\right), \tag{25}$$

where

$$\begin{aligned} &A_1=A(\omega_1)(\omega_2-\omega_1)/2,\\ &A_i=A(\omega_i)(\omega_{i+1}-\omega_{i-1})/2,\quad i=2,\ldots,N-1,\\ &A_N=A(\omega_N)(\omega_N-\omega_{N-1})/2, \end{aligned} \tag{26}$$

are the integrated values of the map in each grid spacing according to a trapezoidal rule of integration and the m_j's are positive parameters derived in analogy with Eq. (26) from the so-called *default* map $m(\omega)$. The unconstrained maximum of the entropy occurs at $\hat{A}_i=m_i$ for which $\hat{S}=0$. The default map $m(\omega)$ is chosen to be consistent with any prior information about the map that is available, we will illustrate its role in the analytic continuation problem later in this section. The form (25) for the entropy has been shown to be the most general form consistent with the axioms of the MEM formalism.[8]

Now we turn to the problem of defining the likelihood probability distribution $\mathscr{P}(D|A)$. In the variables A_j that define a N-dimensional map space and the frequency discretization given above, Eq. (22) assumes the form

$$\mathbf{D}=K\mathbf{A}, \tag{27}$$

where $\mathbf{A}$ and $\mathbf{D}$ are vectors with components A_j and D_i, respectively, and the kernel matrix K, defined as $K_{ij}=K(\tau_i,\omega_j)$, is a linear transformation from the N-dimensional map space to the M-dimensional data space. From a map $\mathbf{A}$ we can, therefore, predict what the data $(K\mathbf{A})_i$ should be and get the residuals from the actual data given. If we exclude the possibility of systematic error, the residuals are due to statistical noise in the data; if we then suppose the errors have Gaussian distributions described by standard deviations σ_i, we have

$$\mathscr{P}(D|A)\propto\prod_{i=1}^{M}\ \exp\left\{-\frac{[D_i-(K\mathbf{A})_i]^2}{2\sigma_i^2}\right\}\equiv\exp\left(\frac{-\chi^2}{2}\right). \tag{28}$$

Combining Eqs. (25) and (28) we see that the *posterior* probability whose maximum is the Maximum Entropy solution to the integral equation (22) is

$$\mathscr{P}(A|D)\propto\exp(\alpha S-\chi^2/2), \tag{29}$$

so that we are left with the problem of maximizing the function of N variables

$$Q(\mathbf{A})=\alpha S(\mathbf{A})-\chi^2(\mathbf{A})/2. \tag{30}$$

A. Selection of the Lagrange multiplier

The arbitrary parameter α in Eq. (24) is interpreted as the inverse Lagrange multiplier in the constrained maximization of S with a fixed value of χ^2. If α is large, the maxi-

mum of $Q(\mathbf{A})$ is dominated by the entropy function, i.e., by the prior information available. Thus, the MEM solution $A(\omega)$ of the integral equation (22) would deviate only slightly from the default map. If, instead, α is small, $A(\omega)$ is determined only by the χ^2 function, and it would then represent very well, in a χ^2 deviation sense, the data. It would also, however, represent any random error present in the data. Thus $A(\omega)$ would be too sensitive to errors in the data, would suffer high oscillations, and it would have little resemblance to the true solution of the integral equation. In the old form of the maximum entropy method, historic maximum entropy, it is a common practice to set α so that, at the maximum of $Q(\mathbf{A})$, $\chi^2=M=$the number of observations. In the most recent form, classic maximum entropy, the best value for α is also derived from Bayesean logic, estimating the maximum of $\mathscr{P}(\alpha|\mathbf{D},m)$, the conditional probability of α given the data and the model map. This is achieved by integrating out A, in a steepest descent approximation, from the expression of the compound probability $\mathscr{P}(A,\alpha|D,m)\propto\mathscr{P}(D|A)\mathscr{P}(A|\alpha,m)\mathscr{P}(\alpha)$ and finding the maximum $\hat{\alpha}$ of the logarithm of the resulting distribution,

$$\ln \mathscr{P}(\alpha|D,m)=\text{const}+\frac{1}{2}\sum_i \ln\left(\frac{\alpha}{\alpha+\lambda_i}\right)+Q(\hat{\mathbf{A}}_\alpha)+\ln \mathscr{P}(\alpha), \tag{31}$$

where $\hat{\mathbf{A}}_\alpha$ is the maximum of $Q(\mathbf{A})$ for the given value of α, $\mathscr{P}(\alpha)$ is the prior probability assigned to the Lagrange multiplier α (usually taken to be proportional to $1/\alpha$ in some finite interval[15]), and λ_i is the ith eigenvalue of the matrix

$$\Gamma_{ij}=\sqrt{A_i}\,\frac{\partial^2(\chi^2/2)}{\partial A_i\,\partial A_j}\,\sqrt{A_j}, \tag{32}$$

evaluated at $\mathbf{A}=\hat{\mathbf{A}}_\alpha$. The maximum of Eq. (31) is approximately given by the equality[15]

$$-2\hat{\alpha}S(\hat{\mathbf{A}}_{\hat{\alpha}})=\sum_i \frac{\lambda_i}{\hat{\alpha}+\lambda_i}. \tag{33}$$

The results shown above and the ones to follow have been obtained assuming, as has been suggested by Skilling,[8] that the metric $\mathscr{G}$ of the map space is the one for which the curvature of the entropy is a constant, i.e., $\mathscr{G}_{ij}=\delta_{ij}/\sqrt{A_iA_j}$, called the *entropic metric*. In this metric a differential volume is $\mathscr{D}A=\Pi_i\, dA_i/\sqrt{A_i}$, the components of a gradient are multiplied by $\sqrt{A_i}$ and the elements of a matrix of second derivatives are multiplied by $\sqrt{A_iA_j}$.

B. Error rescaling

Often the uncertainties σ_i of the data are harder to estimate than the data itself. Since the parameter $\hat{\alpha}$ depends indirectly on σ_i through the eigenvalues of the curvature matrix of χ^2, it is useful to introduce an additional parameter γ that multiplies each σ_i and then estimate its best value $\hat{\gamma}$ using similar techniques used to estimate $\hat{\alpha}$. The result is two simultaneous equations for the $(\hat{\alpha},\hat{\gamma})$ pair

$$\begin{aligned} -2\hat{\alpha}S(\hat{\mathbf{A}}_{\hat{\alpha}})&=\sum_i \frac{\lambda_i}{\hat{\gamma}^2\hat{\alpha}+\lambda_i},\\ \frac{\chi^2(\hat{\mathbf{A}}_{\hat{\alpha}})}{\hat{\gamma}^2}+\sum_i \frac{\lambda_i}{\hat{\gamma}^2\hat{\alpha}+\lambda_i}&=M, \end{aligned} \tag{34}$$

where the λ_i are the eigenvalues of the matrix (32). This procedure, called error rescaling,[15,13] is important to perform correctly the maximum entropy inversion and to assess the quality of the data. In the applications presented in this work we found $1.1<\hat{\gamma}<1.6$.

C. Selection of the default map

Often, the prior information on the map is available in the form of a certain number N_B of sum rules that can be expressed as

$$B_q=\sum_k b_{qk}m_k, \quad q=1,\ldots,N_B. \tag{35}$$

If $\overline{B_q}$ are the known numerical values of the sum rules and δB_q the correspondent uncertainties, we can apply the maximum entropy formalism to obtain the unique default map $m(\omega)$ that satisfies the sum rules (35) within specified error level. The χ^2 deviation to be used is

$$\chi^2=\sum_{q=1}^{N_B}\frac{(B_q-\overline{B_q})^2}{\delta B_q^2}. \tag{36}$$

This procedure would seem to require that we specify a default map for $m(\omega)$. To avoid this we use a normalized form of the entropy

$$S=-\int d\omega\,\frac{m(\omega)}{\mathscr{M}}\ln\frac{m(\omega)}{\mathscr{M}}\simeq-\sum_i p_i\ln\frac{p_i}{\Delta\omega_i}, \tag{37}$$

where $\mathscr{M}=\int d\omega m(\omega)\simeq\Sigma_i m_i$ and $p_i=m_i/\Sigma_i m_i$.

Often N_B is a small number (in the applications presented here we identified two or three useful sum rules) and, for such small dataset, the classic maximum entropy method cannot be used because the best value for the Lagrange multiplier α would be poorly defined. We used instead the historic maximum entropy selection criterion whereby α is chosen to achieve the condition $\chi^2=N_B$. We observed that the default maps derived in this way are nearly independent on the particular value of α selected as long as it is reasonably chosen.

D. Estimation of integrals of the map

The width of posterior probability at its maximum, quantified by the Hessian matrix $\partial^2 Q/\partial\mathbf{A}\,\partial\mathbf{A}$ for the map $\mathbf{A}$, provides information on the uncertainty associated with the maximum entropy inversion. We are often interested in quantities that are related to integrals of $A(\omega)$. Such quantities can be expressed in the form

$$B=\sum_i b_iA_i=\mathbf{b}\cdot\mathbf{A}, \tag{38}$$

and we seek an estimate of the uncertainty δB associated with B. This is more easily accomplished by diagonalizing the Hessian with an orthogonal transformation O and expressing $\mathbf{b}$ in this new basis. If q_i is the i-th eigenvalue of $\partial^2 Q/\partial \mathbf{A}\,\partial \mathbf{A}$ and b_i' the correspondent transformed component of $\mathbf{b}$, the uncertainty δB is given by[13]

$$\delta B^2 = \sum_i \frac{(b_i')^2}{q_i}. \tag{39}$$

From Eq. (39) is clear that if $\mathbf{b}$ has a large component along a direction poorly constrained by the data, the uncertainty of B will be large. On the other hand, if $\mathbf{b}$ has a large component along a direction that is highly constrained, this analysis shows that even relatively low-quality data can accurately generate a particular integrated value of the map. In general, such error analysis provides an invaluable tool to quantify the accuracy of a map inversion and the quantities derived from it.

E. Implementation details

The numerical problem of the constrained maximization of the entropy S has been solved even for very large N (a million or more points on the map) by very efficient algorithms[28] that have been applied successfully to the MEM reconstruction of two-dimensional (2-D) and 3-D images with a large number of pixels. The present application is far less demanding in terms of the dimensionality of the map space because a good representation of the spectral function is described, at most, by a few hundred points. We are able, therefore, to use a safe but memory intensive Newton–Raphson based maximization procedure.[29] Moreover, the linearity of the relation (27) between the map and the data ensures uniqueness of the maximum entropy solution.

In the maximum entropy inversion of the integral equation (8) from PIMC data, we have $D_i = (4\pi^2 e^2/\hbar c) R^2(-i\tau_i)$ and

$$K_{ij} = \frac{\cosh(\beta\hbar\omega_j/2) - \cosh[\beta\hbar\omega_j(1/2 - \tau_j/\beta\hbar)]}{\omega_j \sinh(\beta\hbar\omega_j/2)}, \tag{40}$$

derived from the discretization of the integral equation (8).

As explained in Sec. IV, the data D_i cannot be considered statistically independent. The χ^2 measure needed by the Maximum Entropy inversion algorithm in the case of correlated data is[12]

$$\chi^2 = \sum_{ij} [D_i - (K\mathbf{A})_i](\mathscr{C}^{-1})_{ij}[D_j - (K\mathbf{A})_j], \tag{41}$$

where $\mathscr{C}$ is the cross-correlation matrix of the fluctuations of the data. For the application presented in this paper $\mathscr{C}$ is defined in Eq. (52). We also note that, if the positive definite correlation matrix $\mathscr{C}$ is properly diagonalized by an orthogonal matrix $\mathscr{U}$, the maximum entropy inversion of Eq. (8) can be carried out, starting from the uncorrelated transformed data set $\mathbf{D}' = \mathscr{U}^\dagger \mathbf{D}$ and the transformed linear relation from map space to data space $K' = \mathscr{U}^\dagger K$. The σ_i's in Eq. (28) are, then, interpreted as the eigenvalues of the correlation matrix $\mathscr{C}$.

The default map has been derived, following the procedure presented above, using the sum rules (14), (15), and

$$\frac{4\pi^2 e^2}{\hbar c} R^2\left(\frac{-i\beta\hbar}{2}\right) = \int_0^\infty d\omega\ \sigma(\omega) \frac{\cosh(\beta\hbar\omega/2) - 1}{\omega \sinh(\beta\hbar\omega/2)}. \tag{42}$$

The numerical calculation of the quantities $\langle \mathbf{v}\cdot\mathbf{r}\rangle$ and $\langle \mathbf{v}\cdot\mathbf{v}\rangle$ involved in the sum rules (14) and (15) is described in the next section.

Our maximization algorithm maximizes, in the entropic metric, the function $Q(\mathbf{A})$ (30) with fixed α using the Newton–Raphson method, starting with the initial guess $A_i = m_i$ at the maximum of the entropy function (25) with a large value of α. The inverse Lagrange multiplier α and, eventually, the error rescaling parameter γ are then progressively varied until the self-consistent equations (34) are satisfied. At every iteration convergence is checked by measuring the normalized norm of the difference between the gradient of the entropy and the gradient of the χ^2 function[30] calculated in the entropic metric

$$\delta = \frac{|\alpha\ \boldsymbol{\nabla} S - \boldsymbol{\nabla}(\chi^2/2\gamma^2)|^2}{|\alpha\ \boldsymbol{\nabla} S|^2 + |\boldsymbol{\nabla}(\chi^2/2\gamma^2)|^2}. \tag{43}$$

(For the maximum entropy reconstructed spectra presented in this paper, $\delta < 1\times10^{-4}$.) Quantities related to integrals of the map can then be estimated from Eq. (38) and their uncertainties can be calculated by Eq. (39).

IV. PIMC CALCULATION OF THE IMAGINARY-TIME DATA

The thermodynamic properties of a quantum particle of mass m interacting with a classical solvent can be investigate numerically using the path integral Monte Carlo method (PIMC). This approach exploits the isomorphism between this mixed quantum-classical system and the one in which the quantum particle is replaced by a classical polymer consisting of a large enough number p of beads interacting with their nearest neighbors through harmonic bonds and with the solvent molecules through the interaction potential attenuated by a factor of $1/p$.[31,32]

Notice that the real-time correlation functions obtained by analytic continuation of imaginary-time correlation functions calculated in the classical limit for the solvent degrees of freedom describe the dynamics of the electron in an infinite static disordered lattice of solvent molecules. This is appropriate as long as there is a separation of time scales between the electronic and solvent motions. The static approximation is computationally convenient but not necessary and, by treating the solvent degrees of freedom quantum mechanically in the path integral formalism, it is possible to simulate phonon assisted dynamics.

The canonical average of a property $O(\mathbf{r},\mathbf{R}^M)$ of an excess electron in a classical solvent is, therefore,

$$\langle O\rangle = \frac{1}{Q_p(\beta)}\left(\frac{\beta m\omega_p^2}{2\pi}\right)^{3p/2}\int d\mathbf{R}^M\; e^{-\beta\Phi(\mathbf{R}^M)} \times \int d\mathbf{r}_1\cdots d\mathbf{r}_p\,\frac{1}{p}\sum_i\; O(\mathbf{r}_i,\mathbf{R}^M) \times\exp\left\{-\beta\left[\sum_i\left(\frac{m\omega_p^2}{2}(\mathbf{r}_i-\mathbf{r}_{i+1})^2+\frac{V(\mathbf{r}_i,\mathbf{R}^M)}{p}\right)\right]\right\}, \tag{44}$$

where $\mathbf{r}_i$ are the coordinates of the electron beads and $\mathbf{R}^M$ describes the M-degrees of freedom configuration of the solvent. The canonical partition function is

$$Q_p(\beta)=\left(\frac{\beta m\omega_p^2}{2\pi}\right)^{3p/2}\int d\mathbf{R}^M\; e^{-\beta\Phi(\mathbf{R}^M)}\int d\mathbf{r}_1\cdots d\mathbf{r}_p \times\exp\left\{-\beta\left[\sum_i\left(\frac{m\omega_p^2}{2}(\mathbf{r}_i-\mathbf{r}_{i+1})^2 + \frac{V(\mathbf{r}_i,\mathbf{R}^M)}{p}\right)\right]\right\}, \tag{45}$$

where

$$\omega_p^2=\frac{p}{(\beta\hbar)^2}, \tag{46}$$

$\Phi(\mathbf{R}^M)$ is the interaction potential between solvent molecules, and $V(\mathbf{r},\mathbf{R}^M)$ is the interaction potential between solvent molecules and the electron.[2]

As we have seen, a useful correlation function is the mean-square displacement between pairs of points of the chain separated by the imaginary time increment τ[33]

$$R^2(-i\tau)=\langle|\mathbf{r}[-i\tau']-\mathbf{r}[-i(\tau'+\tau)]|^2\rangle, \tag{47}$$

which is independent on the position of the first point corresponding to the imaginary time τ'. The $R^2(-i\tau)$ correlation function is usually evaluated at the points $\tau_j=\hbar\beta j/p$, $j=0,\ldots,p/2$, by the PIMC averages,

$$R^2(-i\tau_j)=\langle\rho_j\rangle, \tag{48}$$

where the estimator ϱ_j is

$$\varrho_j=\frac{1}{p}\sum_{k=1}^{p}\;|\mathbf{r}_k-\mathbf{r}_{k+j}|^2,\quad j=1,\ldots,p/2. \tag{49}$$

As noted in the previous sections Eq. (14) is important to estimate the quantity $\langle\mathbf{v}\cdot\mathbf{r}\rangle$, which is related to the first derivative of $R^2(-i\tau)$ at $\tau=0^+$ (and to the total absorption cross section). We have used the estimator[34]

$$\langle\mathbf{v}\cdot\mathbf{r}\rangle=\frac{i}{\beta\hbar}\left\langle\sum_{k=1}^{p}\;(\mathbf{r}_{k+1}-\mathbf{r}_k)\cdot\mathbf{r}_k\right\rangle. \tag{50}$$

The mean kinetic energy of the electron, directly related to the second sum rule [Eq. (15)], is calculated using either the virial or the primitive estimator.[35]

The values of the $R^2(-i\tau)$ correlation function at different values of τ are not statistically independent; instead, in this application a significant amount of cross correlation is expected. This is best seen by the normalized cross-correlation matrix of the fluctuations $\delta\varrho_j=\varrho_j-R^2(-i\tau_j)$

$$\tilde{\mathscr{C}}_{ij}=\frac{\langle\delta\varrho_i\;\delta\varrho_j\rangle}{\sqrt{\langle\delta\varrho_i^2\rangle\langle\delta\varrho_j^2\rangle}}=\frac{\mathscr{C}_{ij}}{\sqrt{\mathscr{C}_{ii}\mathscr{C}_{jj}}}, \tag{51}$$

where

$$\mathscr{C}_{ij}=\langle\delta\varrho_i\;\delta\varrho_j\rangle/(L-1), \tag{52}$$

ϱ_j is defined in Eq. (49), and L is the number of samples.

The configuration space of the solvent–electron system is sampled using the Monte Carlo method. In every Monte Carlo pass the internal, rotational, and translational degrees of freedom of each solvent molecule are sampled according to the Metropolis algorithm and the configuration of the electron ring is sampled, applying the staging method[36,37] to a large enough number of segments of the ring in order to cover all its length. After equilibration, all the properties of interest have been accumulated for a number of Monte Carlo passes large enough to ensure convergence. In particular, the quantities ρ_j in Eq. (49) have been considered for $j=1,\ldots,j_{\max}$ and block averaged[38] using $L\geqslant 2j_{\max}$ blocks. For every block the average of ρ_j in that block, $\overline{\rho_j^{(b)}}$, is stored, this quantity is used to calculate the cross-correlation matrix $\mathscr{C}$ in Eq. (52). The eigenvector and eigenvalues of $\mathscr{C}$ can be calculated performing a singular value decomposition of the $L\times j_{\max}$ matrix with elements $\{[\overline{\rho_j^{(b)}}-R^2(-i\tau_j)]/\sqrt{L-1}\}$, avoiding, thus, the calculation of $\mathscr{C}$ and its, often unstable, spectral analysis.

V. THE HYDRATED ELECTRON

An excess electron in water has been simulated using the path integral Monte Carlo method at three different temperatures under atmospheric pressure: ($T=298$ K, $\rho=0.997$ g/cm^3), ($T=340$ K, $\rho=0.980$ g/cm^3), and ($T=373$ K, $\rho=0.958$ g/cm^3). The potential of interaction between two water molecules is taken to be a central force potential obtained as a sum of pair potentials between the constituent atoms.[39–41] The internal vibrations of the water molecule are modeled by a set of Morse potentials.[42,43]

The pseudopotential describing the interaction between a water molecule and the electron is an effective potential that reproduces gas phase scattering data over a wide range of impact energies and it is composed of an electrostatic, exchange, and many-body polarization contributions.[44,45]

The potential model described above has been used by Wallqvist *et al.*[45] to calculate the absorption spectrum in the static limit of the hydrated electron by averaging, over several solvent configurations, the dipole transition moments between energy eigenfunctions of the electron calculated on a three-dimensional grid. The position of the resulting calculated absorption band was in agreement with the experiments,[46] although it failed to reproduce the high-frequency tail found experimentally. Another potential model[47] has been shown to reproduce the shape of the ab-

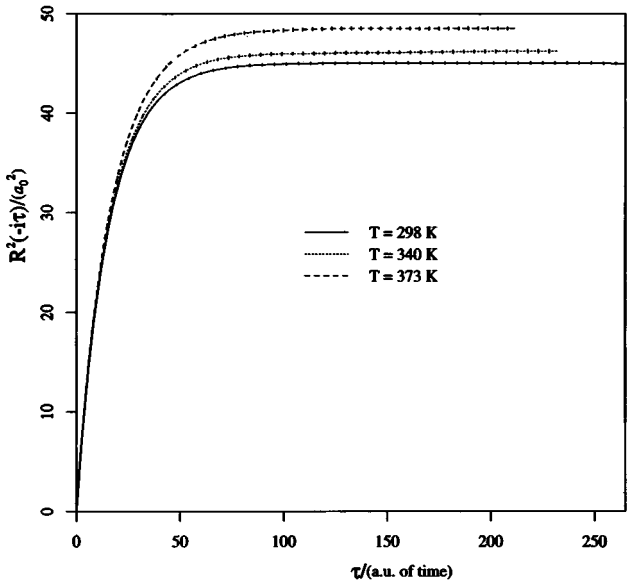

FIG. 1. The imaginary-time displacement correlation function $R^2(-i\tau)$ of hydrated electron at three different temperatures. Error bars are shown every ten calculated points.

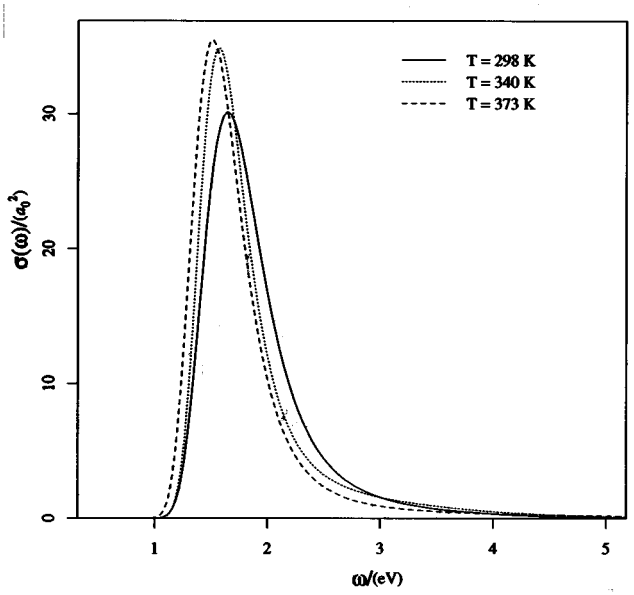

FIG. 2. The calculated absorption spectrum of the hydrated electron at three different temperatures.

sorption band, but not its position. The present calculation should ascertain whether the potential model proposed by Wallqvist *et al.* is capable of reproducing the high-frequency tail by using the computational scheme described in the previous sections.

In our simulation there are 216 water molecules in a cubic box with periodic boundary conditions and of size determined by the chosen liquid density. All interactions above 8 Å have been ignored, implementing a spherical hard cutoff scheme. To calculate the contribution to the many-body polarization energy of an electron bead, only those solvent molecules inside a sphere of radius 5.5 Å centered around it have been considered. Given the numerical complexity associated with evaluating the gradients of the many-body polarization potential, the kinetic energy of the electron has been calculated using the primitive estimator.[35,48,49]

The Trotter number for the electron is $p=900$.[44] The $R^2(-i\tau)$ correlation functions have been calculated calculated for $0<\tau<\beta\hbar/4$ (in the region above this point the correlation function is practically constant and can be ignored without loss of information) by block averaging[38] the estimator ϱ_j in Eq. (49) for $j=1,\ldots,p/4$. The number of blocks, composed of 44 sequential samplings of ϱ_j, was taken to be $L=900$. Thus, about 40 000 Monte Carlo passes were, typically, necessary to ensure proper convergence of the averages.

The imaginary-time displacement correlation functions are shown in Fig. 1 for the three temperatures studied. The corresponding absorption spectra have been calculated by inverting Eq. (8) using the maximum entropy method described in Sec. III and are shown in Fig. 2. The frequency grid used in the maximum entropy numerical inversion has been generated by the expression $\omega(x)=(\omega_{\max}-\omega_{\min})[\exp(ax)-1]/[\exp(a)-1]+\omega_{\min}$, where x is an equally spaced grid of 250 points in the interval $[0,1]$, $a=4$, $\omega_{\min}=0.005$ a.u., and $\omega_{\max}=1$ a.u.

The error rescaling parameter γ has been estimated to lie in the 1.1–1.3 range.

In Fig. 3 we show the comparison between the absorption spectrum of Fig. 2 at 298 K with the the spectrum calculated by Wallqvist *et al.* at 300 K.[45] The agreement is extremely good given the complexity of the model. The noticeable difference is the high-frequency tail present in the present calculation and the experiment but almost absent in the spectra calculated by Wallqvist *et al.*

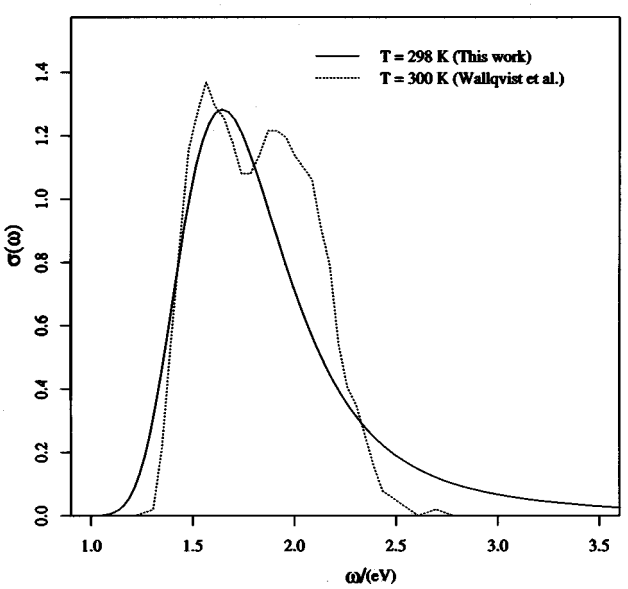

FIG. 3. The calculated spectrum at $T=298$ K of Fig. 2 compared with the absorption spectrum calculated by Wallqvist *et al.* (Ref. 45). In this figure the spectra are normalized by total absorption intensity.

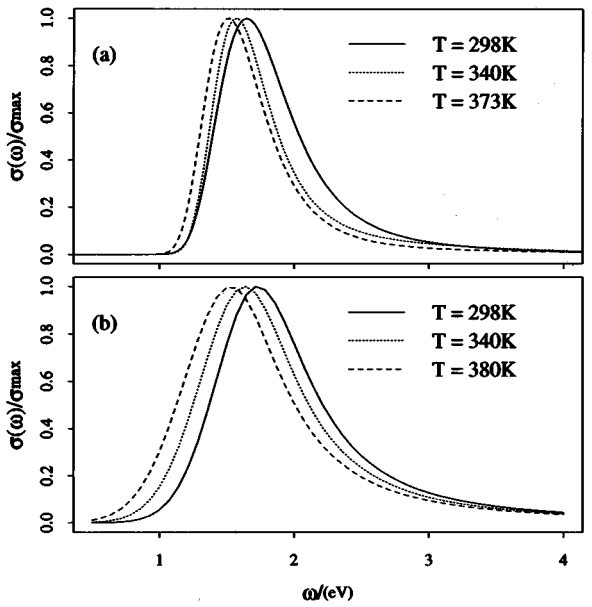

FIG. 4. (a) The calculated spectra of Fig. 2 compared with (b) the available experimental absorption spectra. In this figures the spectra are normalized by the maximum absorption intensity.

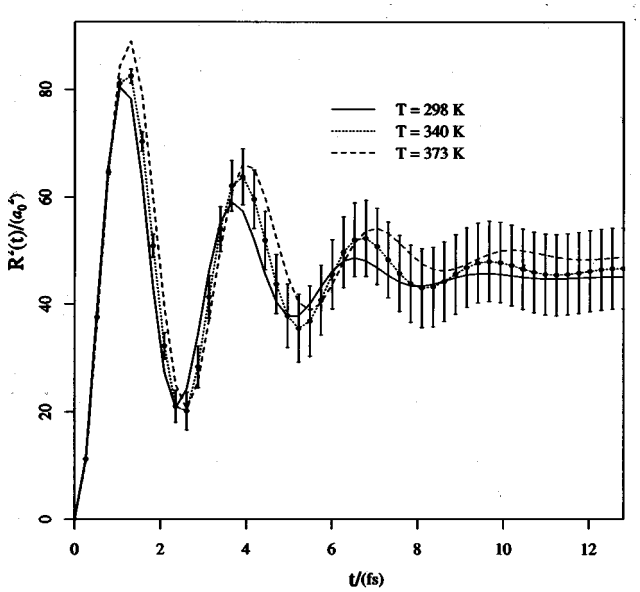

FIG. 5. The real-time displacement correlation functions $R^2(t)$ of a hydrated electron at three different temperatures. Error bars are shown only for the $T=340$ K curve.

In Fig. 4 the maximum entropy-estimated spectra are shown, compared with the experimental spectra,[46] in this figure all the spectra are normalized by the maximum. As can be noticed, the agreement with the experiments is good. The position of the spectrum and its shape is well reproduced, but its width seems to be systematically smaller than the experiments. The change in width with temperature is also in the opposite direction relative to the experiments. We noticed that the width of the absorption band decreased if poorer quality data were used, i.e. data taken from a shorter Monte Carlo simulation. Even though we see a convergence in the shape of the band with increasing simulation length, it is possible that the rate of such convergence is very slow and a very large number of block averages is needed to obtain an accurate bandwidth. It is also possible, and more likely, however, that such features are a consequence of the choice of the pseudopotential made in these calculations as we have observed that an increase the overall cutoff causes a sensible narrowing of the spectral band.

The real-time displacement and velocity correlation functions of the excess electron were calculated from the simulated absorption spectra using Eqs. (7) and (17), and are shown in Fig. 5 and Fig. 6 for the three temperatures studied. The error bars on this function have been calculated, as explained in Sec. III. The displacement correlation functions go flat after a short transient time, showing the fact that the mobility of the electrons is either zero or very small at these conditions. We were not able to determine an accurate value of the electron diffusion coefficient given the present statistical uncertainties.

It should be noted that the present estimate of the electron mobility calculated in a static solvent cannot include the contribution arising from the motion of the solvation cage, a process investigated in a number of classical and semiclassical studies.[4,60] For fluids with very low electron mobility, the motion of the solvent molecules provides the primary mechanism for the diffusion of the electron.

The velocity correlation functions undergo several sign changes before decaying to zero. Thus, it can be concluded that the electron is rattling in a cage of water molecules with which the electron ''collides'' periodically, reversing its velocity. The initial value of the velocity correlation function is the mean square velocity, a measure of the average kinetic energy of the electron. The values obtained are consistent

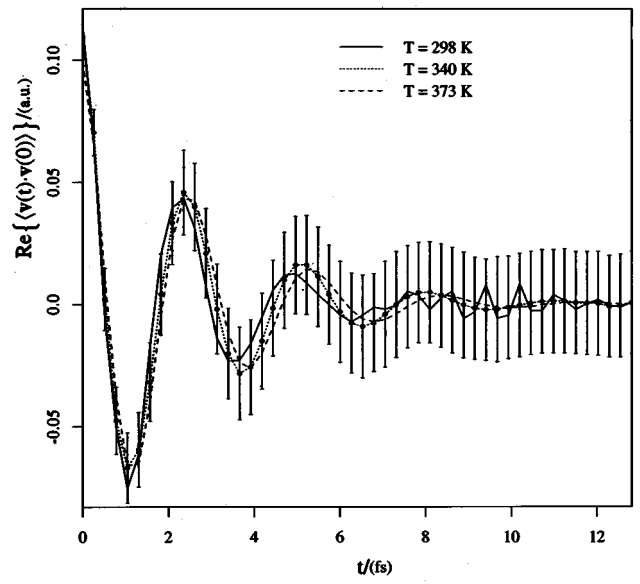

FIG. 6. The real-time velocity correlation functions $\langle \mathbf{v}(t)\cdot\mathbf{v}(0)\rangle$ a of hydrated electron at three different temperatures. Error bars are shown only for the $T=340$ K curve.

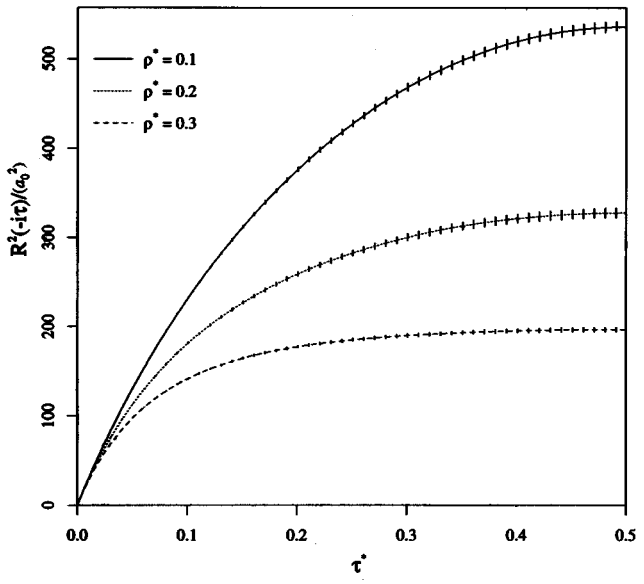

FIG. 7. The imaginary-time displacement correlation function $R^2(-i\tau)$ of an excess electron in supercritical helium at three reduced solvent densities.

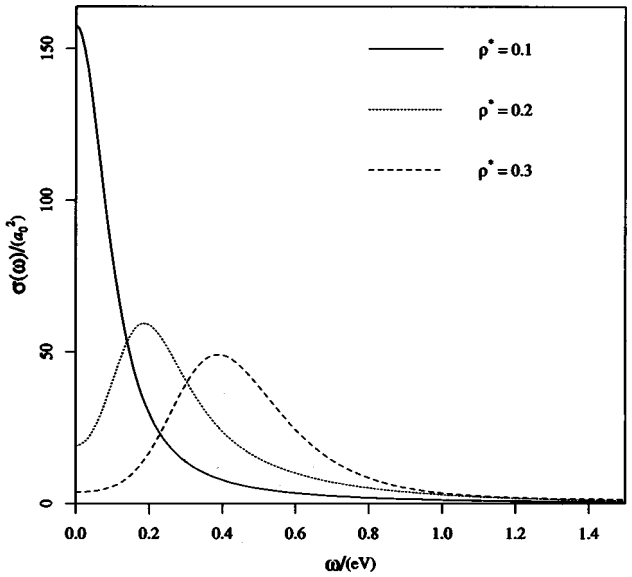

FIG. 8. The calculated absorption spectra of an excess electron in supercritical helium at three reduced solvent densities.

with the ones obtained from the primitive kinetic energy estimator, but with uncertainties two to three times smaller.

VI. AN EXCESS ELECTRON IN SUPERCRITICAL HELIUM

To study the process of electron localization due to the excluded volume effect,[50] we have simulated by path integral Monte Carlo, an excess electron in helium along the 309 K supercritical isotherm at three densities ($\rho^*=\rho\sigma^3=0.1$, 0.2, and 0.3). The potential of interaction between two helium atoms is taken as a Lennard-Jones 12-6 potential ($\sigma=2.556$ Å, $\epsilon=10.22$ K). The electron-helium pseudopotential used is that of Kestner *et al.*,[51] a model used in the past.[52,14] The kinetic energy of the electron has been calculated using the virial estimator.[35]

The simulation is of 864 helium atoms and a discretized electron path in a cubic box with periodic boundary conditions and of size determined by the chosen density. The Trotter number for the electron is $p=1000$.[52] The $R^2(-i\tau)$ correlation functions have been calculated calculated for $0<\tau<\beta\hbar/2$ by block averaging,[38] the estimator ϱ_j in Eq. (49) for $j=1,\ldots,p/2$. The number of blocks, composed of 44 sequential samplings of ϱ_j, was taken to be $L=1200$. Thus, about 50 000 Monte Carlo passes were, typically, necessary to ensure proper convergence of the averages.

The imaginary-time displacement correlation functions are shown in Fig. 7 for the three densities studied. The corresponding absorption spectra were calculated by the maximum entropy inversion of the integral equation (8) using a frequency grid given by the expression $\omega(x)=(\omega_{\max}-\omega_{\min})[\exp(ax)-1]/[\exp(a)-1]+\omega_{\min}$, where x is an equally spaced grid of 250 points in the interval [0,1], $a=4$, $\omega_{\min}=0$, and $\omega_{\max}=1$ a.u.

The calculated absorption spectra, shown in Fig. 8, are in good agreement with previous calculations[14] that used the same potential model for the electron-helium system but a different selection scheme for the Lagrange multiplier in the maximum entropy inversion. As has already been noticed,[14] the observed variations of the absorption bands with density are in agreement with the analytical predictions of the RISM-polaron theory of Chandler and co-workers[53,54] for the hard sphere solvent model of electron solvation.

At the $\rho^*=0.3$ density the absorption spectrum is made of a single band centered around $\overline{\omega}=0.4$ eV of Gaussian shape on the low-frequency side and of Lorentian shape on the high-frequency side, as we have observed for the hydrated electron. This observation correlates well with the fact that in both cases the electron is best described as being localized in a solvent cavity. The absorption band is due to optical transitions from the ground state to localized low-lying excited states.

At lower density ($\rho^*=0.2$) the absorption maximum redshifts, and we can observe a substantial increase of the absorption at zero frequency. From these observation we conclude that under these thermodynamic conditions the electronic ground state and the low-lying excited states are still localized in a solvent cavity but the extended states become thermally accessible, providing means for the electron to diffuse in the solvent.

At the smallest density studied ($\rho^*=0.1$) the absorption band at positive frequencies virtually disappears and the zero frequency absorption becomes more intense. The absorption spectrum therefore assumes a structure similar to the absorption spectrum of an excess electron in xenon investigated in the next section. This is consistent with the fact that at this density the solvent is not able to provide a cavity that supports an electron ground state and few low-lying excited states. At these conditions the electron is best described as being fully delocalized.

From the calculated absorption spectra, using Eq. (7), we

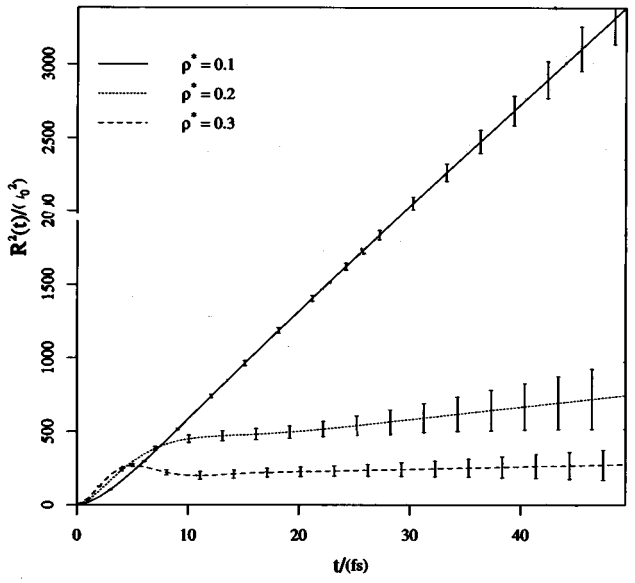

FIG. 9. The real-time displacement correlation functions $R^2(t)$ of an excess electron in supercritical helium at three different reduced densities. Error bars are shown every three calculated points. The asymptotic slope of these curves at large t is proportional to the diffusion coefficient of the electron.

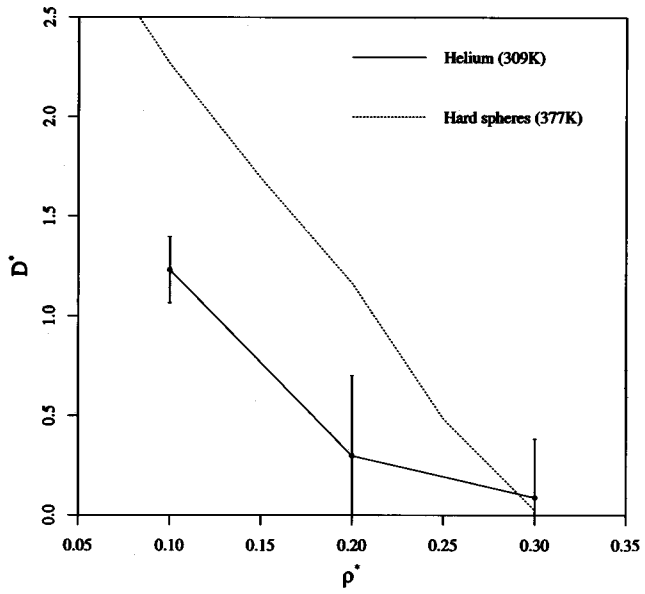

FIG. 10. The calculated reduced diffusion constant $D^*=\beta\hbar\rho^*D/\sigma^2$ of an excess electron in supercritical helium. For helium $\sigma=2.556$ Å. Also shown in a dotted line, the reduced diffusion constant of an excess electron in hard sphere solvent of sphere diameter σ.

have extracted the real-time displacement correlation functions up to 50 fs. These are shown in Fig. 9. Apart from a short-time transient behavior, we observe diffusive motion for times larger than about 25 fs for all the densities studied. This is also in agreement with the predictions of Nichols and Chandler.[54] The diffusive motion sets up at shorter times as the density is lowered. The slope of these functions at long times are proportional to the diffusion coefficient of the electron. The value of the slopes calculated at 50 fs, taken to be our operational definition of the diffusion coefficient, agrees to a 1% tolerance with the asymptotic value at $t=\infty$ given by the zero-frequency absorption cross section [see Eq. (21)]. The error bars in Fig. 9, calculated as explained in Sec. III, provide a mean to estimate the uncertainties of the operational values of the diffusion coefficient by simply considering the upper and lower bounds of the slope of the real-time displacement correlation functions.

The values of the diffusion coefficients are plotted versus solvent density in Fig. 10. In this figure we also show the curve corresponding to the diffusion coefficient for the associated hard sphere model[54] at a slightly larger temperature (377 instead of 309 K). We observe that the two models are in reasonable agreement, suggesting that, in this case, the operational diffusion constants calculated from the slope at 50 fs of the real-time displacement correlation functions are a good representation of the true diffusion constants.

VII. AN EXCESS ELECTRON IN SUPERCRITICAL XENON

An excess electron in supercritical xenon has been simulated using the path integral Monte Carlo method along the 309 K supercritical isotherm for four densities ($\rho^*=\rho\sigma^3=0.3$, 0.5, 0.7, and 0.9). The potential of interaction between two xenon atoms is taken as a simple Lennard-Jones 12-6 potential ($\sigma=4.0551$ Å, $\epsilon=229$ K).[52] The electron–xenon pseudopotential we have used has been developed by Space *et al.*[55] to reproduce the observed s-wave phase shifts in electron-xenon scattering experiments. A many-body polarization term has been added through a Lekner polarization potential.[56] For the calculation of the kinetic energy of the electron we used the virial estimator.[35]

The simulation is of 864 xenon atoms and an electron in a cubic box with periodic boundary conditions and of size determined by the chosen solvent density. The Trotter number for the electron path $p=1000$.[52] The $R^2(-i\tau)$ correlation functions have been calculated calculated for $0<\tau<\beta\hbar/2$ by block averaging[38] the estimator ϱ_j in Eq. (49) for $j=1,\ldots,p/2$. The number of blocks, composed of 44 sequential samplings of ϱ_j, was taken to be $L=1200$. Thus, about 50 000 Monte Carlo passes were, typically, necessary to ensure proper convergence of the averages.

The imaginary-time displacement correlation functions are shown in Fig. 11 for the four densities studied. The corresponding absorption spectra, calculated by the maximum entropy inversion of the integral equation (8) are shown in Fig. 12. The peak intensities occur at $\omega=0$ with a fast-decaying unstructured tail at positive frequencies. The frequency grid used in the maximum entropy numerical inversion has been produced from the expression $\omega(x)=(\omega_{\max}-\omega_{\min})[\exp(ax)-1]/[\exp(a)-1]+\omega_{\min}$, where x is an equally spaced grid of 250 points in the interval [0,1], $a=5$, $\omega_{\min}=0$, and $\omega_{\max}=1$ a.u. The value of the absorption spectrum at $\omega=0$, as we have already noticed, is related to the drift mobility of the electron $\mu_D=e\beta D$, where D is the diffusion coefficient.

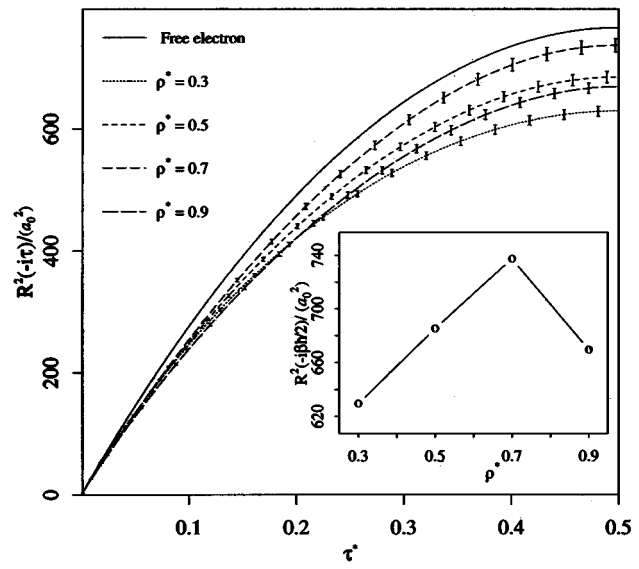

FIG. 11. The imaginary-time displacement correlation function $R^2(-i\tau)$ of an excess electron in supercritical xenon at four reduced solvent densities. The inset shows the variation with density of the value of $R^2(-i\beta\hbar/2)$.

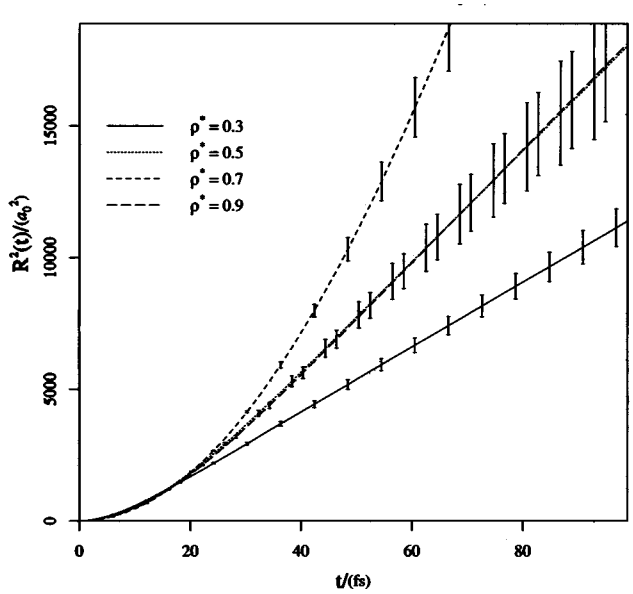

FIG. 13. The calculated real-time displacement correlation functions $R^2(t)$ of an excess electron in supercritical xenon at four reduced solvent densities. The asymptotic slope of these curves at large t is proportional to the diffusion coefficient of the electron.

The error rescaling parameter γ has been estimated to lay in the 1.1–1.3 range.

From the calculated absorption spectrum, using Eq. (7), we have extracted the real-time displacement correlation functions up to 100 fs. These are shown in Fig. 13 only in the 0–50 fs region. Apart from a short-time transient behavior, we observe diffusive motion for times larger than about 25 fs for all the densities studied. The slope of these functions at long times are proportional to the diffusion coefficient of the electron. The value of the slopes calculated at 50 fs are our operational definition of the diffusion coefficient. The statistical uncertainties of these values of the diffusion coefficients has been estimated, as illustrated in Sec. VI. The calculated drift mobilities $\mu_D = e\beta D$, shown in Fig. 14 versus reduced solvent density, present a maximum for $\rho^* = 0.7$.

It is interesting to compare in Fig. 15 the calculated mobilities with the available measurements along the liquid–gas coexistence curve.[57,58] The experimental mobility reaches a maximum of 6000 $cm^2/V\,s$ at $T = 223$ K and $\rho^* = 0.8$, which is in reasonable agreement with the calculated mobilities. The simulations, however, do not reproduce the dramatic fall off of the mobility with decreasing density. At the critical

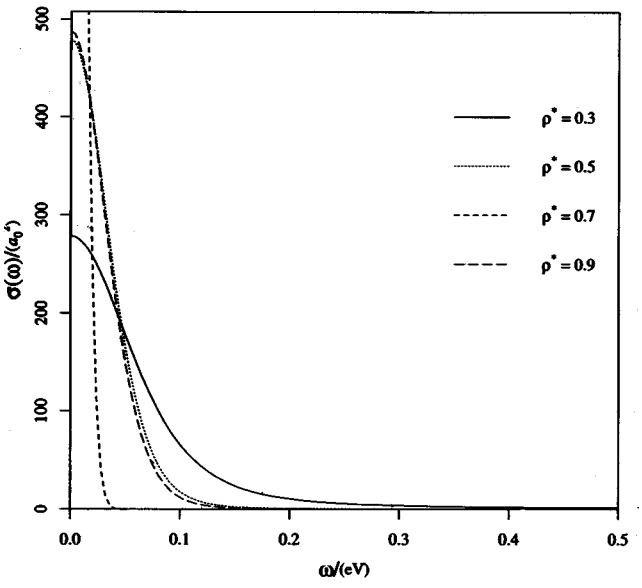

FIG. 12. The calculated absorption spectra of an excess electron in supercritical xenon at four reduced solvent densities.

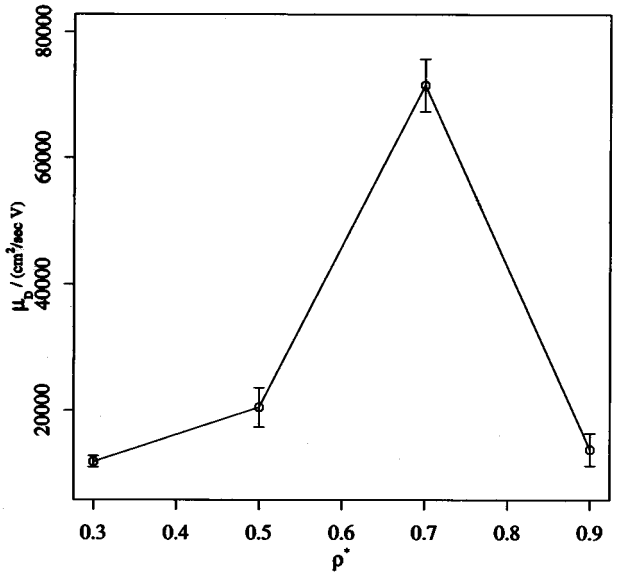

FIG. 14. Calculated drift mobility of an excess electron in supercritical xenon as a function of reduced solvent density.

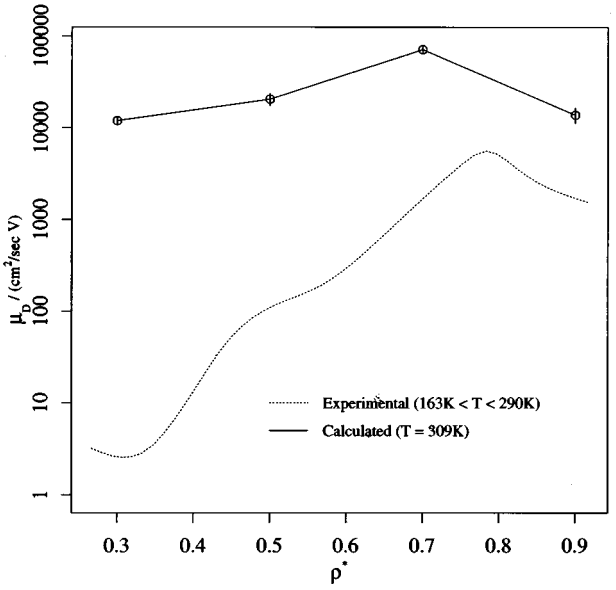

FIG. 15. The calculated mobilities of an excess electron in supercritical xenon at four reduced solvent densities compared with the available experimental measurements along the liquid–gas coexistence curve.

point, $T=290$ K and $\rho^*=0.333$, the measured mobility is just 3.0 cm^2/V s, more than three orders of magnitude smaller than the calculated value at similar thermodynamic conditions ($T=309$ K and $\rho^*=0.3$).

Since the calculations have not been performed along the liquid–vapor coexistence line, but along the 309 K isotherm, the deviations between the experiments and the present calculations can be partially explained by the fact that it is experimentally observed in xenon that even a slight removal of the system from the liquid–vapor coexistence region can sensibly increase the electron drift mobility;[57] this effect is greater the closer the system is to the critical point.

At high densities the electron mobility is large because the energy gap between the localized ground state and the conduction band is comparable to kT. On the other hand, as the critical point is approached large density fluctuations occur and the probability of finding large localizing traps for the electron increases. Then, none of the states in the conduction band will be thermally accessible from the localized ground state, resulting in a small mobility. Hsu *et al.*[59] have observed that the main contributions to this critical behavior come from the large-wavelength fluctuations of the solvent density. Given the finite size of the simulation box, the PIMC simulations performed in this work cannot reproduce density fluctuations with wavelengths of the order of the box size or larger. The simulations, therefore, are not accurate in describing the phenomenon of electron localization near the critical point, a fact that could explain the large deviation between the experimental and calculated mobility at low densities.

The term ''quasilocalized'' is sometimes used to describe the states of the localized electron in liquids of polarizable rare gases because the traps have a size comparable to the De Broglie wavelength of the electron. In a PIMC simulation, thus, the average size of the electron polymer in such a trap will be almost free-particle like. This is in contrast with the fact that a free particle has ballistic motion (infinite diffusion coefficient) while a trapped electron can diffuse only by infrequent hopping from one trap to another. This observation suggests that another contribution to the observed deviation between calculated and experimental drift mobilities may come from the failure of the numerical analytical continuation method to discriminate between a localized electron in a large trap and a ''quasi-free'' extended electron. The absorption spectrum of a localized electron in a large trap is expected to have a peak at very low frequencies whose intensity falls rapidly to zero at zero frequency. Thus, given that the maximum entropy inversion of Eq. (8) has a finite frequency resolution dictated by the precision of the imaginary-time data, a very intense peak at a frequency smaller than the attainable frequency resolution, would be virtually indistinguishable from an absorption at zero frequency. This would result in an overestimation of the mobility of the quasilocalized electron.

To analyze this phenomenon further, we have performed PIMC simulations of an electron in a large isobaric fluctuating spherical cavity, as defined in Ref. 14. In this localized system the electron has zero drift mobility for any cavity size, even though the electron would look almost like a free particle if studied in imaginary time. The analytical solution of this system and its PIMC simulation have been presented in Ref. 14 and will not be repeated here. Notice, however, that for spherical cavities of the size examined here, the analytical derivation presented in Ref. 14 must be generalized by dropping the assumption of ground state dominance. We have studied the model at the two new smaller external pressures: $P_1=5\times10^{-8}$ a.u. and $P_2=1\times10^{-8}$ a.u. The other parameters of the model are the same as those used in Ref. 14: $\beta=1000$ a.u., $p=$Trotter number$=1000$. The De Broglie wavelength of the electron at this temperature is approximately $\lambda=16$ Å to be compared with the average cavity diameters of about 30 and 40 Å for the two external pressures examined. In Fig. 16 we show the calculated and exact absorption spectra and the corresponding real-time displacement correlation functions for the two pressures examined. Notice that most of the absorption intensity of both spectra lies below $\beta\hbar\omega=5$. This is similar to what we find for an electron in xenon and low-density helium. In comparison, the absorption spectrum of an electron self-trapped in water or high-density helium has a peak $\beta\hbar\omega$ an order of magnitude larger. The maximum entropy reconstructed spectrum for the particle in the spherical cavity at the larger pressure is still fairly accurate: the zero frequency absorption and, correspondingly, the estimated drift mobility is essentially zero, and the reconstructed real-time displacement correlation function agrees extremely well with the exact one. At the smaller pressure, however, we notice that the reconstructed spectrum has a wider absorption band that does not decay to zero at zero frequency. Consequently, the real-time displacement correlation function grows linearly with time, in contrast with the exact one that goes flat after a short transient time. Notice that beyond a certain time the calculated error

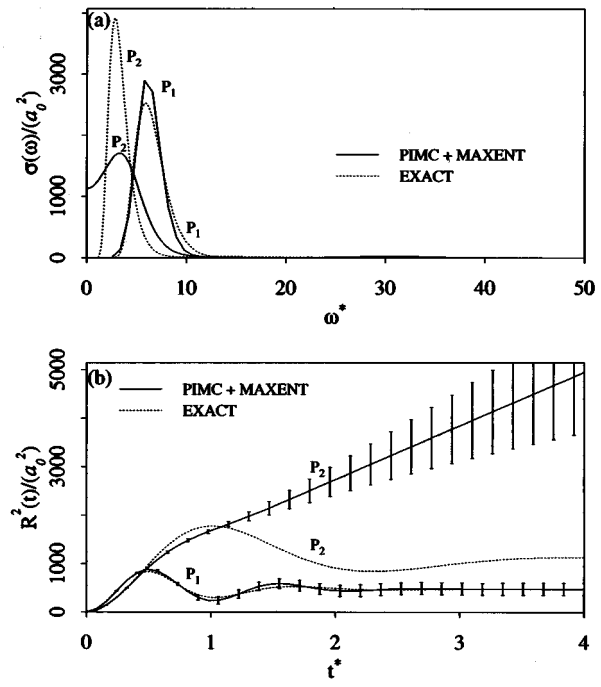

FIG. 16. (a) Absorption cross sections of an electron in a breathing spherical cavity. $\omega^*=\beta\hbar\omega$. (b) The real-time displacement correlation functions $R^2(t)$ corresponding to the absorption spectra shown in (a). $t^*=t/\beta\hbar$. In this figure the curves are labeled according to the external pressures: $P_1=5\times10^{-8}$ a.u. and $P_2=1\times10^{-8}$ a.u. For the values of the other parameters see the text.

bars on the maximum entropy reconstructed correlation function for the lower-pressure case do not include the exact values, this seems to suggest that the analytic continuation in this case is also very sensitive to systematic errors present in the imaginary-time data.

We conclude, therefore, that, although the calculated absorption spectra at finite frequencies and the real-time correlation functions at short times can be still be considered quantitatively accurate, the maximum entropy analytic continuation method is inaccurate in predicting the mobility of a solvated electron trapped, as in xenon near the critical point, in a region of size larger than its De Broglie wavelength.

The issue does not seem to arise in low-density helium, as we found good agreement with the RISM-polaron results[54] for the associated hard sphere model. One reason for this is that the simulations of this system were conducted along the 309 K supercritical isotherm, where critical behavior is not expected to be observed. In this case, thus, we conclude that a sudden drop of absorption intensity at very low frequencies does not occur and the mobility grows as the electron becomes more extended. It is for this reason that in this system the maximum entropy analytic continuation method is able to successfully predict the electron drift mobility.

VIII. CONCLUSIONS

In this paper we have applied the maximum entropy analytic continuation method to the study of dynamical properties of the excess electron in several solvents and in different thermodynamic conditions. Comparing the results of this work with other computational[45] and analytical[54] calculations and with the experiments[57,46] enabled us to test the performance of the method.

The method is very reliable in cases where the electron is localized in a bubble (like in water and supercritical helium at moderate density) in reproducing the absorption spectrum and the real-time position and velocity autocorrelation functions up to times unattainable by most other means. In these cases, however, it is not possible to give an estimate of the values of the mobilities or, equivalently, the diffusion coefficients because they are too small in the static solvent limit. The method can be considered reliable in estimating transport coefficients for extended electrons in low-density helium, where the delocalization is caused by the decrease of the volume excluded to the electron by the solvent.

The method is probably unreliable in reproducing the mobility of excess electrons of polarizable rare gases in the region of the critical point. The source of the problem seems to originate from the combination of finite-size effects in the PIMC simulation that generates the imaginary-time data and from the inability of the analytic continuation method to discriminate between close lying resonance frequencies in the low-frequency region of the absorption spectrum. We believe, however, that even in this case the method provides a good quantitative estimate of the absorption spectra at higher frequencies and of the corresponding real-time correlation functions at short times.

In a future publication we will address the effects of nonadiabatic transitions on the dynamics of electron solvation by treating the solvent coordinates as fully quantal degrees of freedom.

ACKNOWLEDGMENTS

This work was supported by the National Science Foundation (CHE-91-22-506) and the Maui High Performance Computing Center. This paper is in partial fulfillment of the Ph.D. (E.G.) in chemical physics at the Department of Chemistry, Columbia University.

[1] J-P. Jay-Gerin and C. Ferradini, *Excess Electrons in Dielectric Media* (CRC Press, Boca Raton, 1991).
[2] D. F. Coker and B. J. Berne, in *Excess Electrons in Dielectric Media*, edited by J-P. Jay-Gerlin and C. Ferradini (CRC Press, Boca Raton, 1991).
[3] D. Thirumalai and B. J. Berne, Comput. Phys. Commun. **63**, 415 (1991).
[4] J. Schnitker and P. J. Rossky, J. Phys. Chem. **93**, 6965 (1989).
[5] F. Webster, P. J. Rossky, and R. A. Friesner, Comput. Phys. Commun. **63**, 494 (1991).
[6] D. F. Coker. in *Computer Simulations in Chemical Physics*, edited by M. P. Allen and D. J. Tildesley (Kluwer Academic, Dordrecht, 1993), pp. 315–377.
[7] G. Baym and D. Mermin, J. Math. Phys. **2**, 232 (1960).
[8] J. Skilling, in *Maximum Entropy and Bayesian Methods*, edited by J. Skilling (Kluwer Academic, Dordrecht, 1989).
[9] K. Livesey, P. Licinio, and M. Delaye, J. Chem. Phys. **84**, 5102 (1986).
[10] J. Skilling, in *Maximum Entropy in Action* (Kluwer Academic, Dordrecht, 1989).

[11] R. N. Silver, D. S. Sivia, and J. E. Gubernatis, Phys. Rev. B **41**, 2380 (1990).
[12] R. N. Silver, J. E. Gubernatis, and D. S. Sivia, Phys. Rev. Lett. **65**, 496 (1990).
[13] J. E. Gubernatis, M. Jarrell, R. N. Silver, and D. S. Sivia, Phys. Rev. B **44**, 6011 (1991).
[14] E. Gallicchio and B. J. Berne, J. Chem. Phys. **101**, 9909 (1994).
[15] S. F. Gull, in Ref. 8.
[16] B. J. Berne, in *Physical Chemistry, an Advanced Treatise*, edited by H. Eyring (Academic, New York, 1967–1975), Vol. VIII B, Chap. 9.
[17] R. Zwanzig, Annu. Rev. Phys. Chem. **1965**, 67.
[18] J. P. Keener, *Principles of Applied Mathematics* (Addison-Wesley, New York, 1988).
[19] S. W. Provencher and R. H. Vogel, in *Numerical Treatment of Inverse Problems in Differential and Integral Equations*, edited by P. Deuflhard and E. Hairer (Birkhauser, Boston, 1983), p. 304.
[20] C. S. Johnson, Jr., in *Nuclear Magnetic Resonance Probes of Molecular Dynamics*, edited by R. Tycko (Kluwer Academic, The Netherlands, 1994), Chap. 10.
[21] H.-B. Schütter and D. J. Scalapino, Phys. Rev. Lett. **55**, 1204 (1985).
[22] H.-B. Schütter and D. J. Scalapino, Phys. Rev. B **34**, 4744 (1986).
[23] S. R. White, D. J. Scalapino, R. L. Sugar, and N. E. Bickers, Phys. Rev. Lett. **63**, 2504 (1989).
[24] R. M. Bevensee, *Maximum Entropy Solutions of Scientific Problems* (Prentice–Hall, Englewood Cliffs, NJ, 1993).
[25] S. F. Gull and J. Skilling, IAU/URSI Symposium on Indirect Imaging, Sydney, Australia, 1983.
[26] J. Skilling and S. F. Gull, SIAM Proc. Am. Math. Soc. **14**, 167 (1984).
[27] M. Jarrell and J. E. Gubernatis, Phys. Rep. **269**, 133 (1996).
[28] J. Skilling and R. K. Bryan, Mon. Not. R. Astron. Soc. **211**, 111 (1984).
[29] D. A. Pierre, *Optimization Theory with Applications* (Dover, New York, 1986).
[30] R. K. Bryan, Eur. Biophys. J. **18**, 165 (1990).
[31] D. Chandler and P. G. Wolynes, J. Chem. Phys. **74**, 4078 (1981).
[32] B. J. Berne and D. Thirumalai, Annu. Rev. Phys. Chem. **37**, 401 (1986).
[33] D. Chandler, in *Liquids, Freezing and Glass Transition*, edited by D. Levesque, J. P. Hansen, and J. Zinn-Justin (Elsevier, New York, 1990).
[34] L. S. Shulman, *Techniques and Applications of Path Integration* (Wiley, New York, 1981).
[35] M. F. Herman, E. J. Bruskin, and B. J. Berne, J. Chem. Phys. **76**, 5150 (1982).
[36] E. L. Pollock and D. M. Ceperley, Phys. Rev. B **30**, 2555 (1984).
[37] M. E. Tuckerman, B. J. Berne, G. J. Martyna, and M. L. Klein, J. Chem. Phys. **99**, 2796 (1993).
[38] M. P. Allen and D. J. Tildesley, *Computer Simulations of Liquids* (Clarendon, Oxford, 1987).
[39] H. L. Lemberg and F. H. Stillinger, J. Chem. Phys. **62**, 1677 (1975).
[40] A. Rhaman, F. H. Stillinger, and H. L. Lemberg, J. Chem. Phys. **63**, 5223 (1975).
[41] F. H. Stillinger and A. Rhaman, J. Chem. Phys. **68**, 666 (1978).
[42] J. R. Reimers and R. O. Watts, Mol. Phys. **52**, 357 (1984).
[43] J. R. Reimers and R. O. Watts, Chem. Phys. **85**, 83 (1984).
[44] A. Wallqvist, D. Thirumalai, and B. J. Berne, J. Chem. Phys. **86**, 6404 (1987).
[45] A. Wallqvist, G. Martyna, and B. J. Berne, J. Phys. Chem. **92**, 1721 (1988).
[46] F.-Y. Jou and G. R. Freeman, J. Phys. Chem. **83**, 2383 (1979).
[47] P. J. Rossky and J. Schnitker, J. Phys. Chem. **92**, 4277 (1988).
[48] M. Parrinello and A. Rahman, J. Chem. Phys. **80**, 860 (1984).
[49] J. Cao and B. J. Berne, J. Chem. Phys. **91**, 6359 (1989).
[50] D. Chandler and K. Leung, Annu. Rev. Phys. Chem. **45** (1994).
[51] N. R. Kestner, J. Jortner, M. H. Cohen, and A. Rice, Phys. Rev. A **140**, 56 (1965).
[52] D. F. Coker, B. J. Berne, and D. Thirumalai, J. Chem. Phys. **86**, 5689 (1987).
[53] D. Chandler, Y. Singh, and D. M. Richardson, J. Chem. Phys. **81**, 1975 (1984).
[54] A. L. Nichols, III and D. Chandler, J. Chem. Phys. **87**, 6671 (1987).
[55] B. Space, D. F. Coker, Z. H. Liu, B. J. Berne, and G. Martyna, J. Chem. Phys. **97**, 2002–2021 (1992).
[56] J. Lekner, Phys. Rev. **158**, 130 (1967).
[57] S.-S. Huang and G. R. Freeman, J. Chem. Phys. **68**, 1355 (1978).
[58] F. M. Jacobsen, N. Gee, and G. R. Freeman, Phys. Rev. A **34**, 2329 (1986).
[59] D. Hsu and D. Chandler, J. Chem. Phys. **93**, 5075 (1990).
[60] G. S. Del Buono, P. J. Rossky, and T. H. Murphrey, J. Phys. Chem. **96**, 7761 (1992).